fluids

MDPI

Article

Effects of Surface Roughness on Shock-Wave/Turbulent Boundary-Layer Interaction at Mach 4 over a Hollow Cylinder Flare Model

Matt Garcia [1], Eugene N. A. Hoffman [1], Elijah J. LaLonde [1], Christopher S. Combs [1,*], Mason Pohlman [2], Cary Smith [2], Mark T. Gragston [2] and John D. Schmisseur [2]

[1] Department of Mechanical Engineering, Margie and Bill Klesse College of Engineering and Integrated Design, The University of Texas at San Antonio, San Antonio, TX 78249, USA
[2] Department of Mechanical, Aerospace, and Biomedical Engineering, The University of Tennessee Space Institute, Tullahoma, TN 37388, USA
* Correspondence: ccombs@utsa.edu

Abstract: Although it is understood that surface roughness can impact boundary layer physics in high-speed flows, there has been little research aimed at understanding the potential impact of surface roughness on high-speed shock-wave/boundary-layer interactions. Here, a hollow cylinder flare model was used to study the potential impact of distributed surface roughness on shock-wave/boundary-layer interaction unsteadiness. Two surface conditions were tested—a smooth steel finish with an average roughness of 0.85 µm and a rough surface (3K carbon fiber) with an average roughness value of 9.22 µm. The separation shock foot from the shock-wave/boundary-layer interaction on the hollow cylinder flare was tracked by analyzing schlieren images with a shock tracking algorithm. The rough surface increased boundary layer thickness by approximately a factor of 10 compared to the smooth case, significantly altering the interaction scaling. Despite normalizing results, based on this boundary layer scaling, the rough surface case still exhibited mean shock foot positions further upstream more than the smooth surface case. Power spectra of the unsteady shock foot location data demonstrated that the rough surface case exhibited unsteady motion with attenuated energy relative to the smooth-wall case.

Keywords: shock-wave/boundary-layer interactions; roughness; boundary layers

Citation: Garcia, M.; Hoffman, E.N.A.; LaLonde, E.J.; Combs, C.S.; Pohlman, M.; Smith, C.; Gragston, M.T.; Schmisseur, J.D. Effects of Surface Roughness on Shock-Wave/Turbulent Boundary-Layer Interaction at Mach 4 over a Hollow Cylinder Flare Model. *Fluids* **2022**, *7*, 286. https://doi.org/10.3390/fluids7090286

Academic Editor: Mehrdad Massoudi

Received: 29 July 2022
Accepted: 19 August 2022
Published: 23 August 2022

1. Introduction

Hypersonic flows can generate high enthalpy conditions along the surface of a vehicle, necessitating the use of novel high-temperature materials with surface architectures that may exhibit roughness [1]. Some high-speed systems also require ablative materials [2] and the ablation process is known to produce non-uniform surface roughness [3,4], striations [5], and cross-hatching [6]. Ablation is a process involving coupled heat and mass transfer that is characterized by the removal of material from a surface by aerodynamic heating. Ablative heat shields have been used to cool and protect space capsules during atmospheric reentry since the earliest days of crewed spaceflight [7]. Ablation is even more likely to introduce distributed roughness on a surface when employing state-of-the-art complex three-dimensional woven composite materials. These materials, such as woven carbon-carbon (C-C) and woven carbon-silicon carbide (C-SiC), present the issue that different components of the composite often ablate at different rates [8,9]. These surface features can then interact with the boundary layer and may lead to the generation of acoustic disturbances, premature turbulent transition, and elevated heat transfer to the vehicle infrastructure [10,11]. Although the effects of roughness and undulating surface topology have been well-documented for low speed flows [12–14] and discrete roughness elements and boundary layer trips in high-speed flows have been investigated in numerous

studies [15,16]—particularly during NASA's return to flight effort [17–19]—there are very few efforts where distributed roughness has been studied in a supersonic flow. A combination of arc jet and ballistic range tests were employed by Reda et al. [20] to study the effect of ablation on boundary layer turbulent transition. Charwat [21] performed extensive studies observing ablation in camphor and naphthalene models in a relatively low-enthalpy Mach 3 flow. More recently, Latin and Bowersox [22,23] collected Schlieren, laser Doppler velocimetry (LDV), hot wire anemometry, and pitot probe data for Mach 2.9 flow over sand paper, a 3D-machined roughness element, and a 2D-machined roughness element. In these studies, boundary layer profiles of the mean flow properties, turbulent statistics, and energy spectra were well-characterized using the various measurement techniques. Similarly, Peltier et al. [24] investigated the effect of diamond-shaped cross-hatching on a Mach 4.9 flow using Schlieren imaging and particle image velocimetry (PIV). Other related work included PIV investigations of distributed roughness by Kocher et al. [25] at Mach 2 and Sahoo et al. [26] at Mach 7.

To further complicate system design, supersonic systems will inevitably experience shock-wave/boundary-layer interactions (SWBLI) that can be generated by fins [27], control surfaces [28], and control jets [29,30]. SWBLI can lead to adverse pressure gradients that are strong enough to produce flow separation while inducing unsteady behavior within the interaction region [31,32]. Given the highly unsteady nature of SWBLI, the resulting elevated heating and pressure loads can put considerable stress on a vehicle design and in some instances lead to catastrophic vehicle failure [33]. SWBLI have been analyzed with a variety of canonical geometries including impinging shocks [34], cylinders [35], and compression ramp shock generators [36] to better understand and classify shock structure across a range of Mach and Reynolds numbers. Considerable effort has been made to characterize the impact of incoming boundary layer state on SWBLI as well, from laminar, to transitional, to turbulent incoming boundary layers [37]. Key flow features within SWBLI have been studied through the analysis of surface-pressure measurements, shock foot location, and high-speed schlieren images while using descriptive statistics among the structures developed within the interaction [38,39]. Structures such as separation shocks can also be visualized and easily identified with schlieren imaging [40]. This large body of work has demonstrated that SWBLI exhibit a characteristic low-frequency unsteadiness that typically resides with a Strouhal number range of 0.01–0.1 [41], with relatively high-energy broadband unsteadiness for turbulent SWBLI and the potential for sharp spectral peaks in the unsteadiness of transitional SWBLI. Even though SWBLI have been studied in detail with a wide body of previous research, there are no known peer-reviewed open access publications that have attempted to characterize the impact of surface roughness on SWBLI.

In the present work, the authors aimed to explore the impact of distributed surface roughness on the structure and dynamics of a fully turbulent SWBLI generated by a hollow-cylinder-flare model in a Mach 4 freestream. Commercially available carbon fiber was selected as a canonical distributed roughness texture to provide a comparison between a smooth and rough surface. Here, an analysis of high-speed schlieren imaging data is provided. Using a custom shock-tracking algorithm, a variety of statistical data on the unsteady shock motion were produced.

2. Experimental Program

2.1. Wind Tunnel Facility

The Mach 4 low-enthalpy Ludwieg Tube facility at the University of Tennessee Space Institute (UTSI) was used to acquire schlieren images for these experiments. This wind tunnel has a test section volume of 610 × 610 × 1830 mm (24 × 24 × 72 in). Unheated dry air is supplied by a compressor into the driver tube with pressures up to 0.48 MPa (~70 psi). Test runs are initiated with the burst of a Mylar diaphragm. The vacuum tank can evacuate 31 m^3 (8200 gal) of air down to 130 Pa (1 Torr). These conditions produce a freestream Mach number of 4 with a freestream unit Reynolds number range of 3.48–50.3 × 10^6 m^{-1} (1.0–16.5 × 10^6 ft^{-1}) and an average freestream velocity of 671 m/s (2201 ft/s). Optical

windows with a viewing area of 280 × 432 mm (11 × 17 in) are located on the test section side walls to provide optical access for experiments [42]. A summary of wind tunnel conditions for this campaign can be found in Table 1. Given the nature of the Ludwieg tube operation using Mylar diaphragms, there is a roughly 15% uncertainty in target burst pressure prior to each test. For this reason, the burst pressures were slightly different between the smooth and rough surface test cases, leading to Reynolds numbers that differed by 12%. However, it is assumed in the present analysis that this change in the Reynolds number had a significantly smaller impact on the interaction when compared to the change in surface texture.

Table 1. UTSI Mach 4 wind tunnel test conditions for the present test campaign.

Case	Stagnation Pressure (kPa)	Static Pressure (kPa)	Stagnation Temperature (K)	Free Stream Velocity (m/s)	Re/x (m^{-1})
Smooth	374	2.9	295	672	17.2×10^6
Rough	427	3.1	299	672	19.7×10^6

2.2. Test Geometries

A hollow cylinder flare model (HCF), as shown in Figures 1 and 2, was used to study the effects of surface roughness on SWBLI in this test campaign. This geometry was chosen in an attempt to provide an axisymmetric quasi-two-dimensional interaction and thus simplify the corresponding analysis while making future simulations more tractable. The HCF included an aluminum flare with an angle of 30° and an adjustable steel body inserted through the flare. The steel body was positioned 320 mm (12.6 in) downstream of the leading edge of the flare to produce an incoming turbulent boundary-layer for the SWBLI based on prior experiments with this model [43]. The hollow cylinder flare model was secured to the bottom plate of the test section plate by the means of a strut. The steel body of the HCF was cleaned thoroughly to remove adhesives from previous testing and maintain a polished surface for the smooth surface test, while 3K woven carbon fiber was applied to the steel body of the HCF with a spray-on adhesive for the rough surface test. The average surface roughness, R_a, was obtained by using a profilometer after preparing both surfaces. Measurements of surface roughness indicated average roughness values of R_a = 0.85 µm and 9.22 µm for the smooth and rough surfaces, respectively. Detailed surface roughness profile data can be provided upon request by emailing the corresponding author.

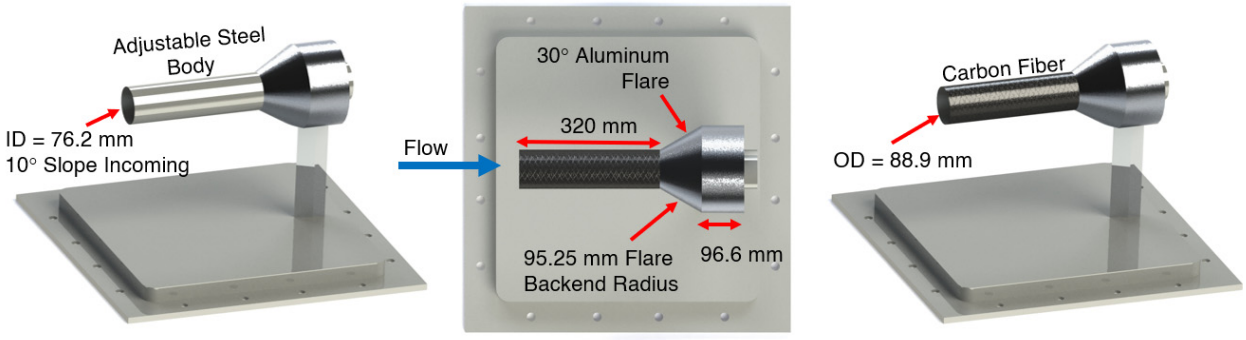

(**a**) (**b**) (**c**)

Figure 1. Dimensional schematics of the hollow cylinder flare model, (**a**) smooth surface, (**b**) top view, and (**c**) rough surface.

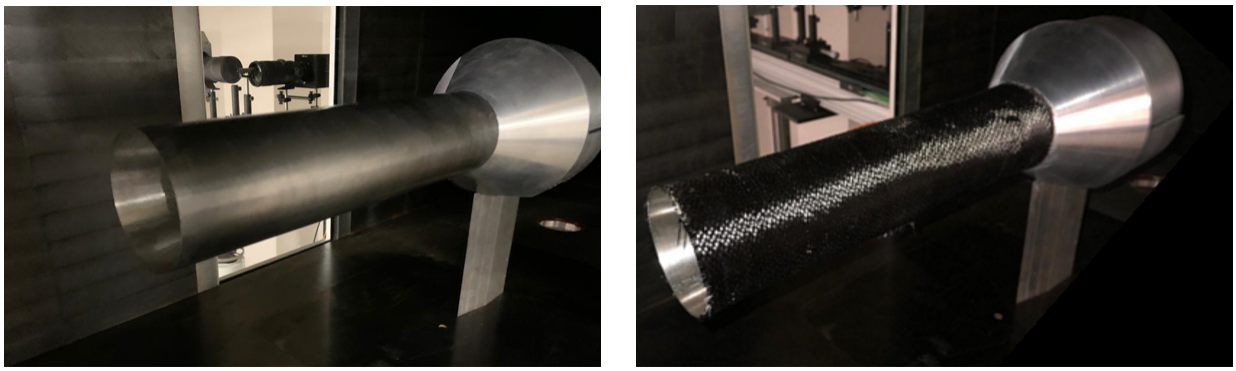

(**a**) (**b**)

Figure 2. (**a**) Smooth surface and (**b**) rough hollow cylinder flare model mounted in the wind tunnel.

2.3. Experimental Setup

Schlieren imaging was employed to obtain high-speed shock foot location data. Schlieren imaging is a non-intrusive visualization technique that provides a visualization of density gradients in a flow. A more in-depth discussion of schlieren imaging is given by Settles [44]. The schlieren system was configured using a Z-type optical setup with 2.54-m-focal-length mirrors. A high-powered, Luminus pulsed light-emitting diode provided high-intensity pulsed light at 200 kHz (duration < 1 µs) to freeze the motion of the shock structures within each image [45]. A horizonal knife edge orientation was used for these experiments to highlight the flow features of interest. Images were acquired using a Photron FASTCAM SA-Z high-speed camera fitted with camera lens systems shown in Table 2. Note that different lenses were used for the two test campaigns considering the vastly different physical scales of the interactions. Over the 70 ms steady-state test period for each test case, the high-speed schlieren system captured 14,000 images.

Table 2. Schlieren imaging details.

Surface	Image Resolution	Acquisition Rate	Scale	Camera Lens
Smooth	640 × 122 pixels	200 kHz	10.95 pixel/mm	300 mm lens + 2x teleconverter
Rough	384 × 176 pixels	200 kHz	2.19 pixel/mm	70–200 mm lens

2.4. Schlieren Image Processing

Schlieren images were imported into a custom MATLAB® script to correct the placement of images and determine the shock foot location, L_s, of the SWBLI [39]. To ensure accurate shock tracking, a reference point was established at the intersection of the HCF body and flare. However, the wind tunnel's vertical and horizonal movement throughout the test run varied the position of the reference point. The wind tunnel motion was corrected and images were stabilized using a 2-D cross-correlation of the image stacks with a reference image using the predetermined reference point. The maximum peak correlation amplitudes in both axes were found and matched with the lag value. The lag values determined the required pixel shift needed to match the location of the refence image in the vertical and horizontal directions. Using the same algorithm previously verified by Combs et al. [39] by comparing image-based shock positions to surface-pressure data, the shock wave position was determined using a threshold-based algorithm that systematically identifies shock position in an image using measured intensity fluctuations in the interaction region. Although the algorithm has been described by Combs et al. [39], we will repeat the description here to make the details available in this open access forum.

The objective of the shock tracking script employed here is to identify the forward lambda-shock, λ_1, in an automated and accurate manner. This is a necessity when acquiring

time-resolved data at 100 kHz, as tens of thousands of images are collected during each run. Furthermore, Cauchy edge detection and simple binary image schemes were found to be insufficient for the current experiments, likely owing to the relative complexity of the flowfield, high turbulent noise in the freestream, and low pixel resolution of the images acquired. The code identifies the location of shock structures through a 9-step process, outlined here:

1. User-assisted definition of flowfield region of interest (ROI) where shock is likely to be located, through a graphical user interface.
2. Rotate ROI image matrix by a user-defined estimated shock angle.
3. Average rotated image matrix in vertical direction.
4. Detect variation (s) in the line resulting from Step 3 to collect approximate location of shock structure center.
5. Transform coordinates of shock center back to ROI image matrix.
6. Based on the estimated shock angle, define a straight line passing through the shock center to serve as an initial estimate.
7. For each shock structure and for each row i in the image matrix, interrogate along a line centered at the location of the initial estimate with bounds $\pm b$, where b is a user-defined window size, and identify the position of each shock in row i by locating the center of the intensity variation along the line.
8. Step 7 produces a shock location for each row in the image matrix. If fewer than five points are identified for a given shock feature, a not-a-number (NaN) result is returned for the image and an error is logged. Otherwise, a straight line is fit to the series of points. If the best-fit solution does not fit within a user-defined shock angle tolerance, a NaN result is returned for the image and an error is logged.
9. Shock positions and angles are logged and (optionally) the result is displayed to the user in real time, and superimposed on the individual schlieren image. Shock location outliers that lie beyond user-defined bounds are also assigned a NaN value and result in an error being recorded.

There are multiple checks that attempt to control the quality of the processed data by removing erroneous values and logging all solution errors. In addition to these automated checks, it has been considered good practice to manually monitor the output of the code (Step 9 option) for at least 100 images to verify the accuracy of the solutions prior to processing an entire data set. Using this procedure, it has been found that when using appropriate user-defined parameters, the algorithm routinely identifies valid shock positions in over 99% of the total images for a given run. An uncertainty analysis accounting for possible errors in the detection of a shock's location yielded a conservative estimate of the uncertainty in instantaneous shock location measurements of $\pm 8\%$.

Figure 3 shows a representative set of images highlighting measured shock locations acquired by the shock tracking portion of the script. Reported shock foot positions are based on the extrapolated location (assuming linear propagation) where the captured shock-wave would impinge on the HCF surface. Frequency spectra of the processed data were computed using the MATLAB® pwelch command with a fast Fourier transform size of 7000 points and a Hamming window with 50% overlap and a frequency resolution, df, of 330 Hz.

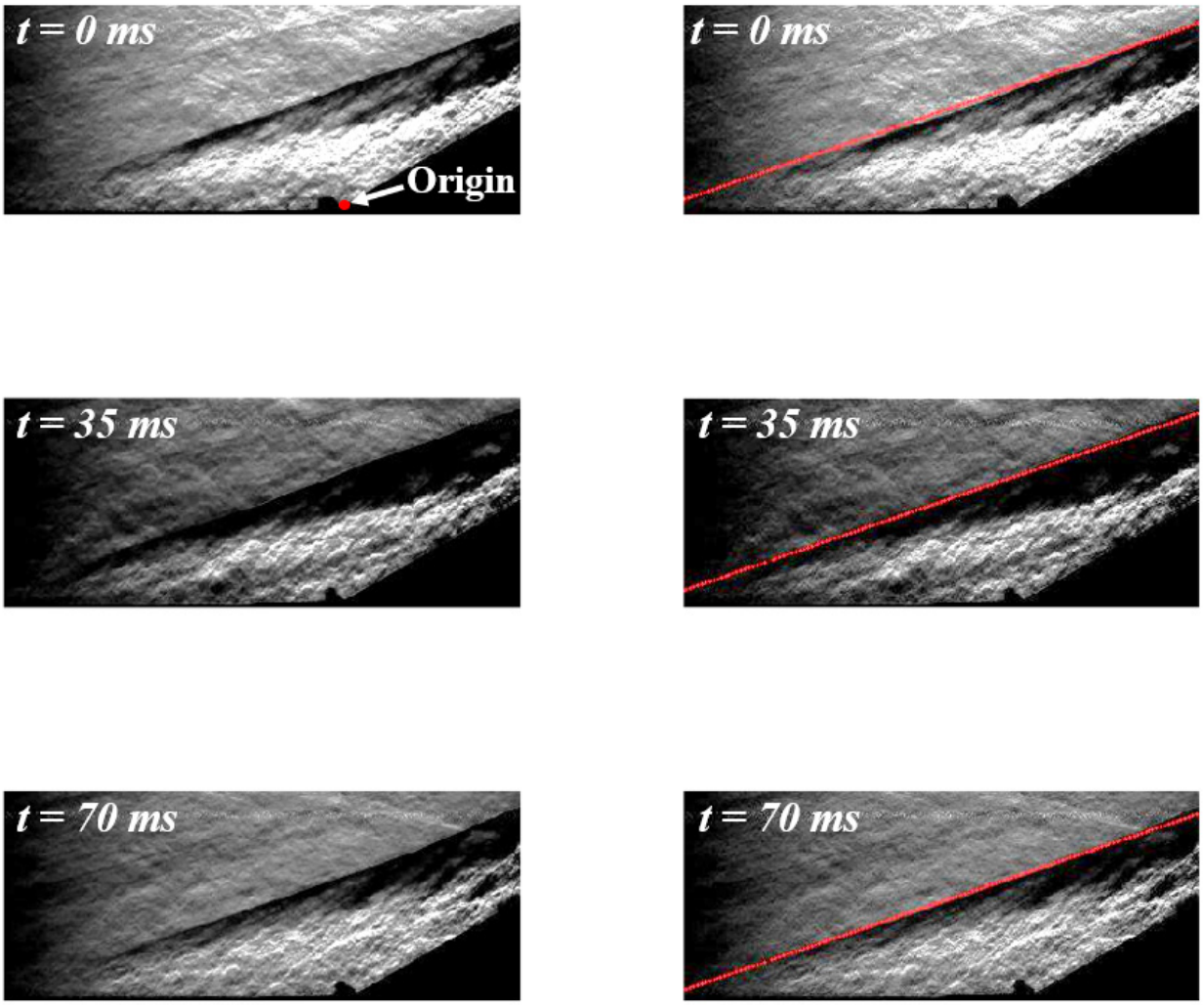

Figure 3. Representative schlieren images demonstrating computed shock positions of rough surface, (**a**) instantaneous images, and (**b**) corresponding shock tracking images.

3. Results and Discussion

Instantaneous and mean images of the two test configurations were obtained from the steady-state portion of individual wind tunnel runs as seen in Figure 4. As the schlieren technique provides a visualization of boundary layer structures, images acquired separately without the flare attachment were used to estimate the incoming boundary layer thickness, δ, and upstream of the interaction region. The boundary-layer heights were estimated at δ = 2.6 $\pm$ 0.2 mm and 11.4 $\pm$ 1 mm for the smooth and rough surfaces, respectively. For the present analysis, this estimation was deemed sufficient considering that the boundary layer heights were simply necessary for image scaling and normalization. The mean images can be used to estimate the mean shock foot location, $L_{\bar{s}}$, by tracing the upper part of the shock-wave down to the surface of the HCF. The shock foot location for the smooth surface can be estimated to lie close to $-5\ x/\delta$, whereas the rough surface shock foot location extends to $-10\ x/\delta$ (cropped out of field-of-view in order to provide same scaling as smooth surface case). The instantaneous images provide a scaling normalized by the boundary-layer height. The out-of-focus circular structure seen just above the shock-wave in the smooth-wall case is due to a dust particle that was deposited on the window during a run (does not impact the flow or the present analysis).

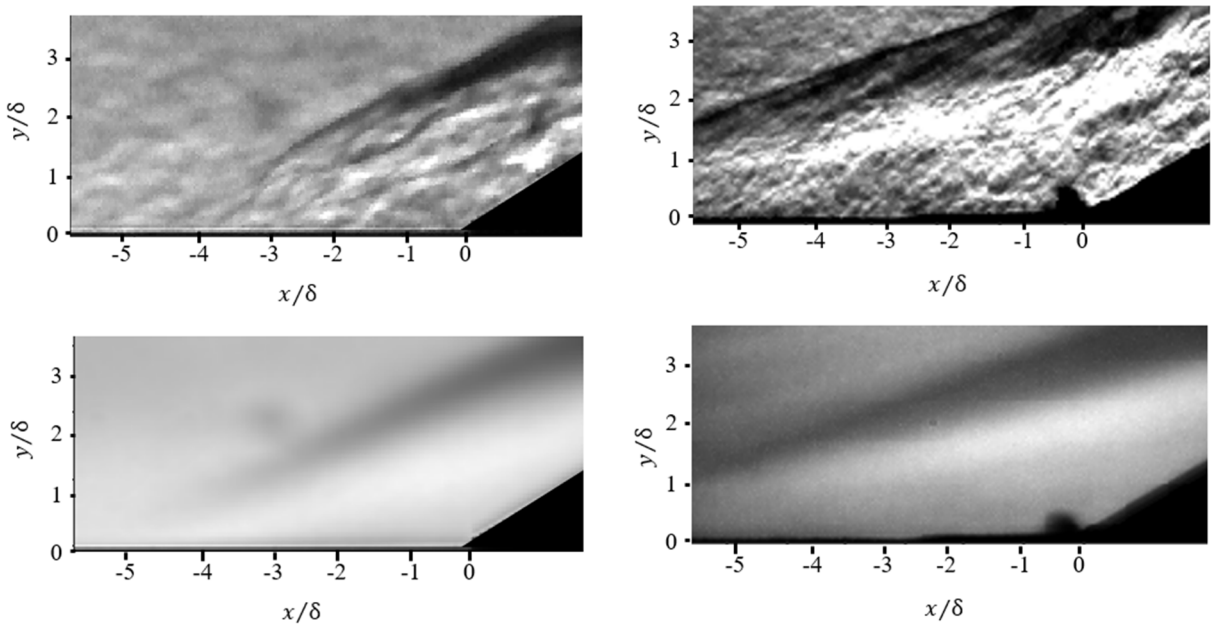

(**a**) (**b**)

Figure 4. Instantaneous (top) and mean (bottom) schlieren visualizations of SWBLI, (**a**) smooth surface, and (**b**) rough surface.

Annotated instantaneous Schlieren images from both surfaces can be seen in Figure 5. The separation shock is clearly visualized for each case upstream of the flare. The area underneath the shock has been established in the SWBLI literature base to contain a separated flow region, a recirculation region, and a corresponding shear layer. Although not apparent in still instantaneous images, these structures can be observed when watching high-speed schlieren animations. The shocks are clearly at different angles even when considering that the scales of the interactions are vastly different. Animations of the Schlieren images also make it clear that the shock structure is highly unsteady. This low-frequency shock unsteadiness was the focus of the analysis presented here.

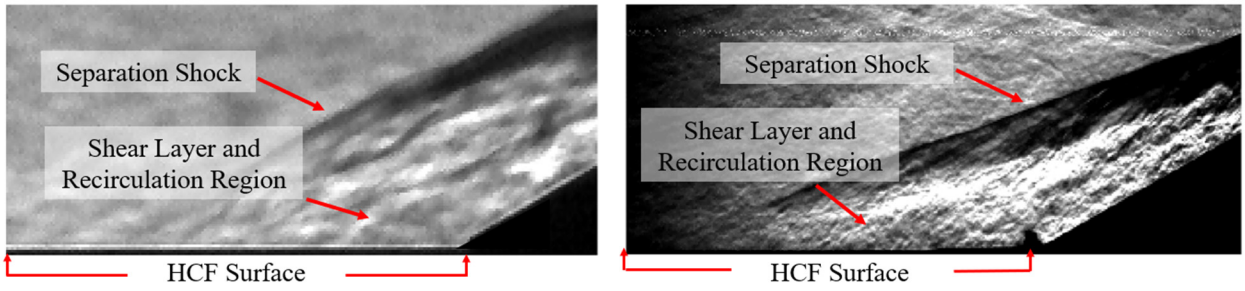

(**a**) (**b**)

Figure 5. Representative schlieren images, (**a**) smooth surface, and (**b**) rough surface.

The pixel-intensity standard deviation (r.m.s.) fields for the smooth and rough surfaces are shown in Figure 6. The *light-colored* sections within the SWBLI indicate higher pixel-intensity-based r.m.s. values. The SWBLI region shows higher variability of pixel intensities compared to the rest of the flow suggesting that the position of the structure fluctuates at a relatively high intensity. Note that the highest intensity region in both cases is *within* the shock structure and not aligned with the mean shock itself. This likely represents a shear layer structure at the edge of the separated flow region. It is also clear from these images that the relative shapes of the rough and smooth interaction are markedly different.

The smooth surface interaction shows a recirculation and interaction region that is much closer to the leading shock. For the rough surface case, the angle of the shock is different (quantified later with shock tracking) and there is notably a larger region of separation between the shear layer feature and the leading shock.

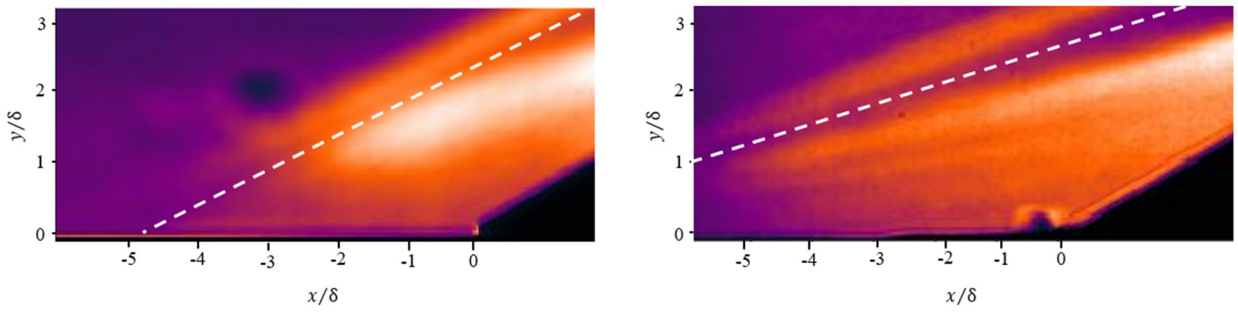

(**a**) (**b**)

Figure 6. RMS fields for SWBLI, (**a**) smooth surface, and (**b**) rough surface. The white dashed lines indicate the mean shock position for each case.

Figure 7a shows the tracked shock foot location data as a function of time. The rough surface time series demonstrates that the shock foot location is further away from the origin when compared to the smooth surface, as observed in the Schlieren images. The histogram normalized as a probability density function, P (X), provided in Figure 7b, confirms the mean shock foot location, $L_{\bar{s}}$, is found to be -5 and -10 x/δ for the smooth and rough surfaces, respectively. Furthermore, the rough surface data are distributed throughout a wider range of positions when compared to the smooth surface as evidenced by a higher standard deviation value (1.49δ vs. 0.98δ) as shown in Table 3. Additionally, both data sets possess a slight right-handed skewness. This is seen noticeably within the rough shock foot position data as this structure exhibited a longer tail in the downstream direction (closer to the flare). The shock angles were found to be 20° and 29° for the rough and smooth surface, respectively. A summary of the shock-motion statistics is provided in Table 3.

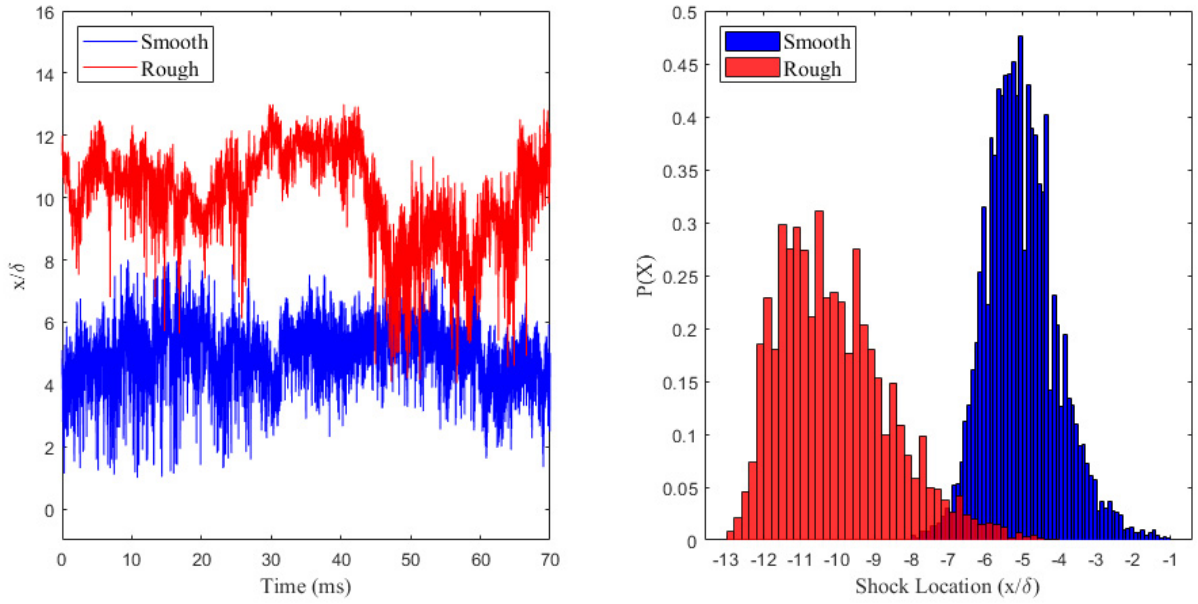

(**a**) (**b**)

Figure 7. (**a**) Normalized shock foot location time series, and (**b**) histogram normalized as a PDF of smooth and rough SWBLI mean shock foot location.

Table 3. Summary of shock-motion using descriptive statistics.

Surface	R_a (μm)	δ (mm)	θ (deg)	L_i (mm)	L_s (x/δ)	σ	σ^2	Kurtosis	Skewness
Smooth	0.85	2.6	29	12	−5	0.98	0.97	4.3	−0.55
Rough	9.22	11.4	20	71	−10	1.49	2.23	3.4	−0.77

Shock intermittency, γ_{L_s}, was calculated using the shock-tracking data and is shown in Figure 8a. The intermittency is defined as:

$$\gamma_{L_s}(x) = \frac{\sum_{i=1}^{N} x(L_{s,i}) < x}{N} \quad (1)$$

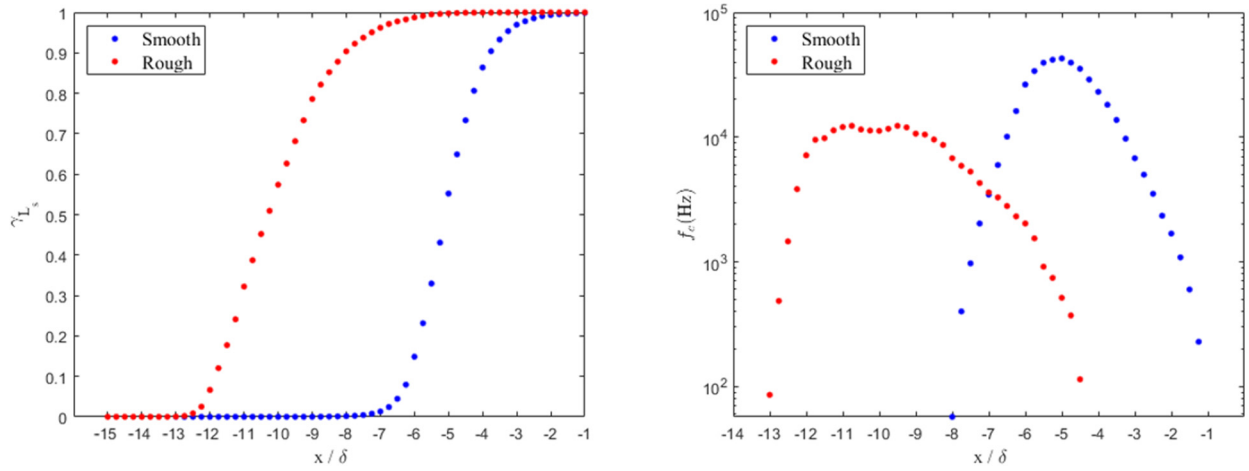

(**a**) (**b**)

Figure 8. (**a**) Intermittency of the rough and smooth surfaces' L_s, and (**b**) zero-crossing frequency of the shock foot location for smooth and rough surfaces.

The intermittent region, L_i, can be determined by locating the position interval where the shock foot has an intermittency of unity and zero. In other words, the intermittent region can be considered to be the range of locations where the shock is at times present. The intermittency of the rough surface is shown to be within -6 to -12 x/δ, whereas the smooth surface lies within -2 and -7 x/δ. This indicates that an increase of surface roughness will move the interaction further upstream while creating a larger intermittent region.

Figure 8b shows the zero-crossing frequency, f_c, of the shock foot position. The zero-crossing frequency is defined as:

$$f_c(x) = 1/\left[\frac{1}{N}\sum_{i=1}^{N} T_i(x)\right], \quad (2)$$

where $T_i(x)$ is the ith shock period in the time series at station x. The zero-crossing frequency analysis similarly indicates that the SWBLI will be further upstream as the surface roughness increases. Furthermore, the peak zero-crossing frequency for the smooth and rough surfaces lie at -5 and -10 x/δ upstream of the ramp with a magnitude of 40 kHz and 10 kHz, respectively. This indicates that the smooth surface SWBLI shock foot traverses the mean location at a higher frequency than the rough SWBLI shock foot.

One-sided autospectral-density functions, $G(f)$, were calculated for both shock foot location test cases. As is convention in the SWBLI literature base, the spectral energy was normalized by "pre-multiplying" by frequency and dividing by the variance. The spectral signature of the shock-motion is shown in Figure 9a. Upon inspection, the spectral energy of the signals is notably different and the coherence, γ_{xy}^2, in Figure 9b confirms that the

signals do not possess similar spectral signatures. The rough shock foot data possesses a peak spectral energy between 6 and 10 kHz with a steadily decreasing energy signature for higher frequencies. The smooth shock foot data exhibits a PSD signature that gradually increases with increasing frequency with no apparent peaks. This increase with respect to frequency is likely an artifact of the pre-multiplication scaling; however, it is possible that oscillations for the smooth case are centered at lower frequencies that are difficult to measure in an impulse wind tunnel facility owing to the relatively short test times. Nevertheless, this analysis demonstrates that the SWBLI dynamics for the two cases are considerably different. Figure 9c,d present these results in terms of the Strouhal number, *St*, using two different length scales: the intermittent region length and the incoming boundary layer height. Whereas much of the previous literature for compression ramp interactions employed a Strouhal number scaling based on the intermittent length of the shock interaction, this scaling produces surprisingly high peak Strouhal numbers (~1) for the rough surface in the present work. This may indicate that the intermittent length is not the appropriate scaling factor for the HCF interaction studied here. For comparison, the incoming boundary layer thickness was also used, which indicated a peak intensity of *St*~0.1 for the rough surface SWBLI, which is more in-line with the low-frequency unsteadiness observed in previous work.

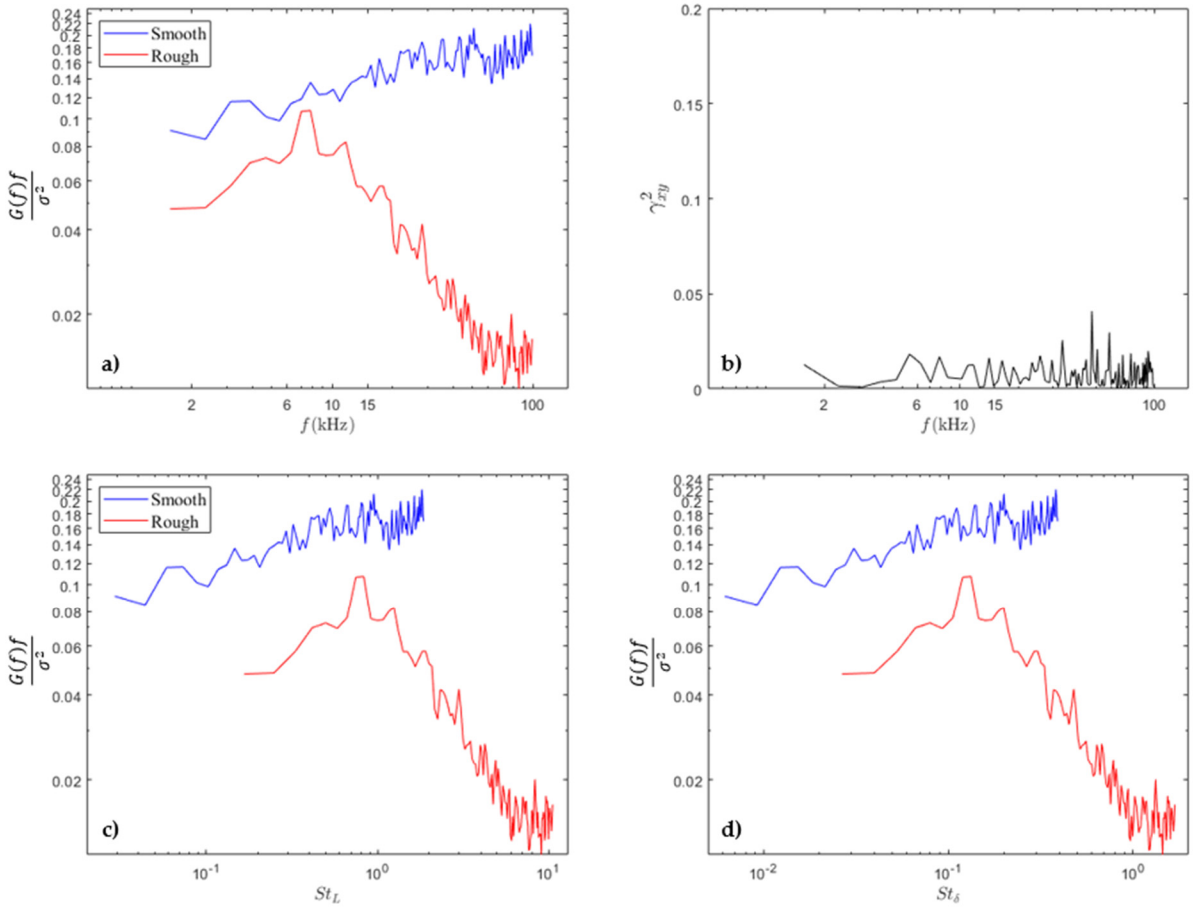

Figure 9. (**a**) Power spectral density of shock location versus frequency, (**b**) coherence for rough and smooth surface, (**c**) power spectral density of shock location versus Strouhal number (intermittent length scaling), (**d**) power spectral density of shock location versus Strouhal number (boundary layer thickness scaling).

Instabilities within the Schlieren image sequence can also be shown by the Strouhal number images in Figure 10. As done by Combs et al. [38], a representative Strouhal number value was calculated for each pixel by identifying the peak frequency at each individual

location based on the instantaneous fluctuation of the Schlieren image intensity. The results were plotted on a colormap within a range of zero to unity on a log scale. Both surfaces show a Strouhal number approaching unity in the freestream region as would be expected. In general, lower Strouhal number values are seen in the vicinity of the shock structure and in the separated flow region. These values correspond to the relatively low-frequency shock unsteadiness that has been observed to occur near St ~0.01–0.1. It is interesting to observe that although a low-frequency peak was not observed in the PSDs of the smooth-surface shock tracking data, the low-frequency unsteadiness is evident in Figure 10. Meanwhile, for the rough surface SWBLI case, the low-frequency unsteadiness is more confined to the shock structure. There appears to be some higher-frequency unsteadiness inside the shock structure and the shear layer or separated flow region for the rough surface case.

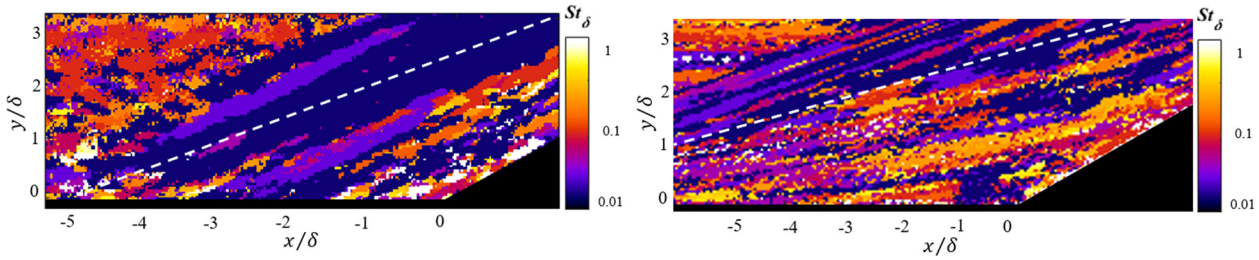

(**a**) (**b**)

Figure 10. Plots of Strouhal number in the interactions region for representative (**a**) smooth and (**b**) rough interactions. The white dashed lines indicate the mean shock positions for each case.

In addition to calculating the power spectra of the shock position data, normalized one-sided autospectral density functions were calculated for the Schlieren image sequences on a per-pixel basis. As done by Combs et al. [38] for cylinder-generated SWBLI and similar to the analysis presented in Figures 11 and 12, a PSD was computed for each pixel where the amplitudes were integrated over five frequency bands. The resulting amplitudes were normalized by multiplying the frequency spacing used in the calculation (df) and then dividing by the variance of the intensity field for a given image sequence. The values were plotted over a colormap to represent the average spectral energy content per pixel over a specified frequency band. Figures 11 and 12 show the spectral energy content split between bands of 1–2, 2–6, 6–10, 10–15, and 15–100 kHz. The power spectra of the shock foot location data are provided next to each respective two-dimensional power spectra as a means to compare the spectral energy of the shock foot to the overall spectral energy in the flow. Comparing both two-dimensional power spectra, it is shown that most of the spectral energy is concentrated between the 1–2 and 2–6 kHz bands. The spectral energy in the proceeding frequency bands is lower, demonstrating that the unsteadiness of the SWBLI is highest within the 1–2 and 2–6 kHz bands. When comparing the shock foot power spectra along the two-dimensional spectra, both surfaces have a similar spectral energy distribution when compared to the two-dimensional spectral images. However, it is notable that the rough and smooth cases exhibit markedly different energy signatures, suggesting that the SWBLI physics are impacted by the change in surface texture.

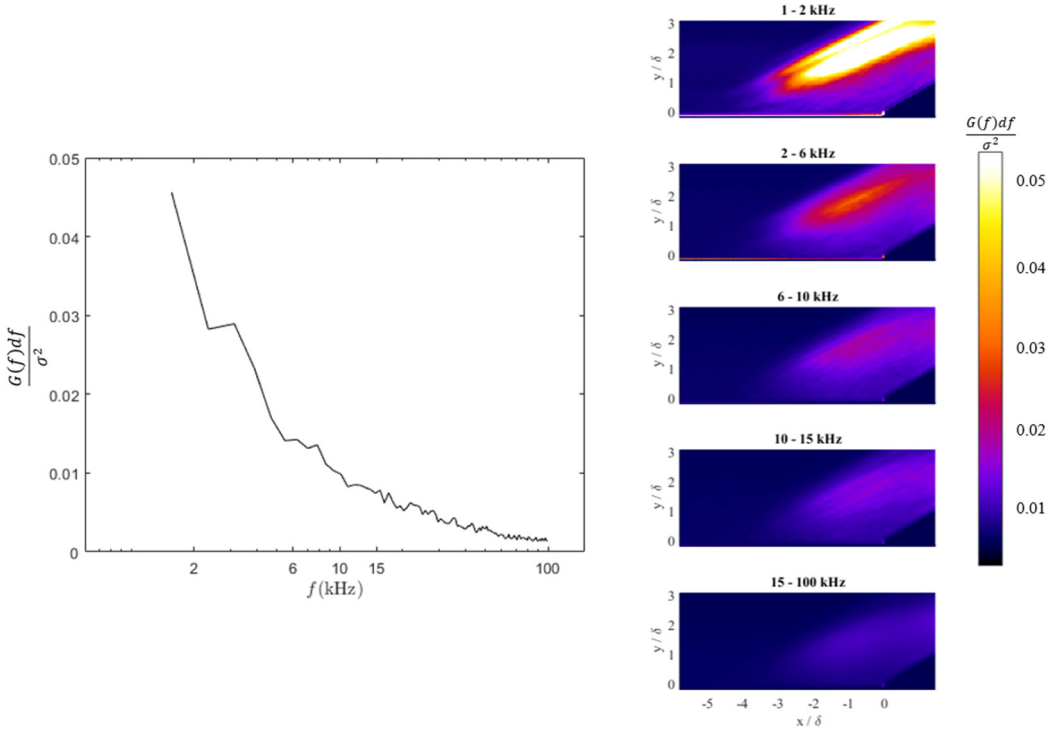

Figure 11. Normalized power spectra of high-speed schlieren images, averaged over different frequency bands for smooth surface.

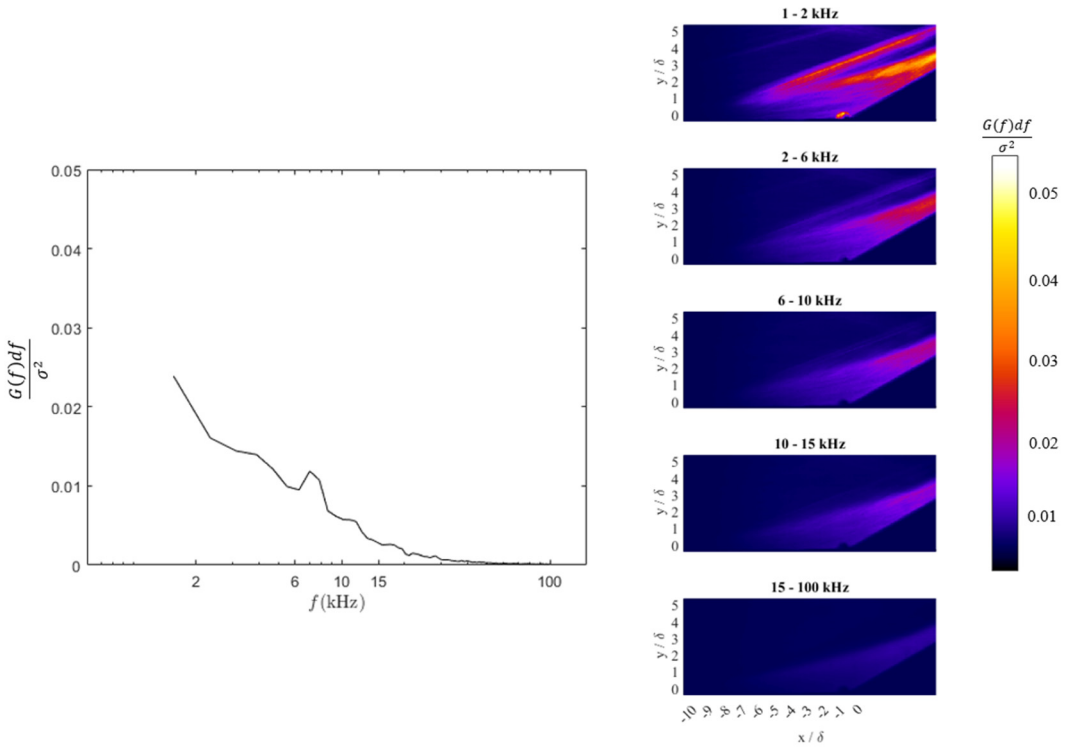

Figure 12. Normalized power spectra of high-speed schlieren images, averaged over different frequency bands for rough surface.

4. Conclusions

An experimental study on the effects of surface roughness within a shock-wave/boundary-layer interaction (SWLBI) at the Mach 4 Ludwieg Tube facility in University

of Tennessee Space Institute (UTSI) was performed. Schlieren images of the two surfaces were obtained to analyze the unsteadiness of the SWBLI. The instantaneous and mean images of the two surfaces produced an approximation for the shock foot location, L_s, be -5, and -10 x/δ for the smooth and rough surface tests, respectively, using a probability density function. The spectral energy analysis suggests that the two interactions are notably different in both the mean and unsteady sense. The rough surface produces a peak in spectral energy between 6 to 10 kHz whereas an energy peak was not observed for the smooth surface case (perhaps below the available measurement threshold). The shock foot intermittent region, L_i, is 71 mm and 12 mm of the rough and smooth surface, respectively, suggesting that an increase in surface roughness increases the intermittency of the separation shock. The max zero-crossing frequency, f_c, was 40 kHz for the smooth surface SWBLI and 10 kHz for the rough surface SWBLI. When analyzing images on a per-pixel basis, it was evident that low-frequency unsteadiness dominated the shock motion and separated flow region dynamics. Computed Strouhal number values for shock motion fell within the range of 0.1–1, which are consistent with the archival literature. However, the power-spectral density profiles of the rough vs. smooth interaction cases were considerably different and the rough-wall case exhibited an attenuated energy signature when compared to the smooth-wall case.

Author Contributions: Conceptualization, C.S.C. and J.D.S.; methodology, C.S.C. and J.D.S.; software C.S.C., M.G., E.N.A.H. and E.J.L.; formal analysis, C.S.C., E.N.A.H. and M.G.; investigation, E.N.A.H., M.G., M.P. and C.S.; data curation, M.G.; writing—original draft preparation, M.G., E.N.A.H. and E.J.L.; writing—review and editing, C.S.C.; visualization, M.G.; supervision, C.S.C., C.S., M.T.G. and J.D.S.; project administration, C.S.C. and J.D.S.; funding acquisition, C.S.C. and J.D.S. All authors have read and agreed to the published version of the manuscript.

Funding: This material is based upon work supported by the Air Force Office of Scientific Research under award number FA9550-20-1-0190 and by the U. S. Office of Naval Research under award number N00014-15-1-2269. Additional support was also provided by NASA grant number 80NSSC19M0194.

Institutional Review Board Statement: Not applicable.

Informed Consent Statement: Not applicable.

Data Availability Statement: To obtain data from this study please contact the corresponding author.

Acknowledgments: Thank you to Jose Rodriguez for helping obtain the experimental data.

Conflicts of Interest: The authors declare no conflict of interest. The funders had no role in the design of the study; in the collection, analyses, or interpretation of data; in the writing of the manuscript; or in the decision to publish the results.

References

1. Radespiel, R.; Ali, S.R.C.; Muñoz, F.; Bowersox, R.; Leidy, A.; Tanno, H.; Kirk, L.C.; Reshotko, E. Experimental Investigation of Roughness Effects on Transition on Blunt Spherical Capsule Shapes. *J. Spacecr. Rocket.* **2019**, *56*, 405–420. [CrossRef]
2. Combs, C.S. Quantitative Measurements of Ablation-Products Transport in Supersonic Turbulent Flows Using Planar Laser-Induced Fluorescence. Ph.D. Dissertation, The University of Texas at Austin, Austin, TX, USA, 2015.
3. Siddiqui, F.; Gragston, M.; Saric, W.S.; Bowersox, R.D.W. Mack-mode instabilities on a cooled flared cone with discrete roughness elements at Mach 6. *Exp. Fluids* **2021**, *62*, 213. [CrossRef]
4. Siddiqui, F.; Saric, W.S.; Bowersox, R.D. Interaction of Second-Mode Disturbances and 3-D Roughness on a Cooled Flared Cone at Mach 6. In Proceedings of the AIAA Scitech 2021 Forum, Virtual, 11–21 January 2021. [CrossRef]
5. Stock, H.W.; Ginoux, J.J. Experimental results on crosshatched ablation patterns. *AIAA J.* **1971**, *9*, 971–973. [CrossRef]
6. Berg, D.E. Surface Roughness Effects on the Hypersonic Turbulent Boundary Layer. Ph.D. Dissertation, California Institute of Technology, Pasadena, CA, USA, 1977.
7. Sietzen, F., Jr. From Mercury to CEV: Space Capsules Reemerge. *Aerosp. Am.* **2005**, *43*, 26–30.
8. Vignoles, G.L.; Lachaud, J.; Aspa, Y.; Goyhénèche, J.-M. Ablation of carbon-based materials: Multiscale roughness mod-elling. *Compos. Sci. Technol.* **2009**, *69*, 1470–1477. [CrossRef]
9. Chawla, K.K. *Composite Materials Science and Engineering*; Springer Science & Business Media: Berlin/Heidelberg, Germany, 1989. [CrossRef]

10. Stern, E.C.; Poovathingal, S.; Nompelis, I.; Schwartzentruber, T.E.; Candler, G.V. Nonequilibrium flow through porous thermal protection materials, Part I: Numerical methods. *J. Comput. Phys.* **2019**, *380*, 408–426. [CrossRef]
11. Poovathingal, S.; Stern, E.C.; Nompelis, I.; Schwartzentruber, T.E.; Candler, G.V. Nonequilibrium flow through porous thermal protection materials, Part II: Oxidation and pyrolysis. *J. Comput. Phys.* **2019**, *380*, 427–441. [CrossRef]
12. Wu, Y.; Christensen, K.T. Outer-layer similarity in the presence of a practical rough-wall topography. *Phys. Fluids* **2007**, *19*, 085108. [CrossRef]
13. Wu, Y.; Christensen, K.T. Spatial structure of a turbulent boundary layer with irregular surface roughness. *J. Fluid Mech.* **2010**, *655*, 380–418. [CrossRef]
14. Mejia-Alvarez, R.; Christensen, K.T. Low-order representations of irregular surface roughness and their impact on a turbulent boundary layer. *Phys. Fluids* **2010**, *22*, 015106. [CrossRef]
15. Berry, S.A.; Auslender, A.H.; Dilley, A.D.; Calleja, J.F. Hypersonic Boundary-Layer Trip Development for Hyper-X. *J. Spacecr. Rocket.* **2001**, *38*, 853–864. [CrossRef]
16. Jiang, N.; Webster, M.; Lempert, W.R.; Miller, J.D.; Meyer, T.R.; Ivey, C.B.; Danehy, P.M. MHz-rate nitric oxide planar laser-induced fluorescence imaging in a Mach 10 hypersonic wind tunnel. *Appl. Opt.* **2010**, *50*, A20–A28. [CrossRef] [PubMed]
17. Dyakonov, A.; Danehy, P.; Garcia, A.; Borg, S.; Berry, S.; Inman, J.; Alderfer, D. Fluorescence Visualization of Hypersonic Flow Past Triangular and Rectangular Boundary-Layer Trips. In Proceedings of the 45th AIAA Aerospace Sciences Meeting, Reno, NV, USA, 8–11 January 2007. [CrossRef]
18. Danehy, P.; Bathel, B.; Ivey, C.; Inman, J.; Jones, S. NO PLIF Study of Hypersonic Transition over a Discrete Hemispherical Roughness Element. In Proceedings of the 47th AIAA Aerospace Sciences Meeting, Orlando, FL, USA, 5–8 January 2009. [CrossRef]
19. Bathel, B.; Danehy, P.; Inman, J.; Watkins, A.; Jones, S.; Lipford, W.; Goodman, K.; Ivey, C.; Goyne, C. Hypersonic Laminar Boundary Layer Velocimetry with Discrete Roughness on a Flat Plate. In Proceedings of the 40th Fluid Dynamics Conference and Exhibit, Chicago, IL, USA, 28 June–1 July 2010. [CrossRef]
20. Reda, D.; Wilder, M.; Bogdanoff, D.; Olejniczak, J. Aerothermodynamic Testing of Ablative Reentry Vehicle Nosetip Materials in Hypersonic Ballistic-Range Environments. In Proceedings of the USAF Developmental Test and Evaluation Summit, Woodland Hills, CA, USA, 16–18 November 2004. [CrossRef]
21. Charwat, A.F. *Exploratory Studies on the Sublimation of Slender Camphor and Naphthalene Models in a Supersonic Wind-Tunnel*; Memorandum RM-5506-ARPA; Rand Corp: Santa Monica, CA, USA, 1968. Available online: https://apps.dtic.mil/sti/citations/AD0673531 (accessed on 28 July 2022).
22. Latin, R.M.; Bowersox, R.D.W. Flow Properties of a Supersonic Turbulent Boundary Layer with Wall Roughness. *AIAA J.* **2000**, *38*, 1804–1821. [CrossRef]
23. Latin, R.M.; Bowersox, R.D.W. Temporal Turbulent Flow Structure for Supersonic Rough-Wall Boundary Layers. *AIAA J.* **2002**, *40*, 832–841. [CrossRef]
24. Peltier, S.J.; Humble, R.A.; Bowersox, R.D.W. Crosshatch roughness distortions on a hypersonic turbulent boundary layer. *Phys. Fluids* **2016**, *28*, 045105. [CrossRef]
25. Kocher, B.D.; Kreth, P.A.; Schmisseur, J.D.; LaLonde, E.J.; Combs, C.S. Characterizing Streamwise Development of Surface Roughness Effects on a Supersonic Boundary Layer. *AIAA J.* **2022**, 1–14. [CrossRef]
26. Sahoo, D.; Smits, A.; Papageorge, M. PIV Experiments on a Rough Wall Hypersonic Turbulent Boundary Layer. In Proceedings of the 40th AIAA Fluid Dynamics Conference and Exhibit, Chicago, IL, USA, 28 June–1 July 2010. [CrossRef]
27. Lindörfer, S.A.; Combs, C.S.; Kreth, P.A.; Bond, R.B.; Schmisseur, J.D. Scaling of cylinder-generated shock-wave/turbulent boundary-layer interactions. *Shock Waves* **2020**, *30*, 395–407. [CrossRef]
28. Bathel, B.F.; Jones, S.B.; Watkins, A.N.; Berry, S.; Goodman, K.; Combs, C.S.; Schmisseur, J.D.; Kreth, P.A.; Lash, E.L. Shockwave/Boundary-Layer Interaction Studies Performed in the NASA Langley 20-Inch Mach 6 Air Tunnel. In Proceedings of the AIAA Aviation 2019 Forum, Dallas, TX, USA, 17–21 June 2019.
29. Gaitonde, D.V. Progress in shock wave/boundary layer interactions. *Prog. Aerosp. Sci.* **2015**, *72*, 80–99. [CrossRef]
30. Combs, C.S.; Clemens, N.T.; Danehy, P.M.; Bathel, B.; Parker, R.; Wadhams, T.; Holden, M.; Kirk, B. Fluorescence Imaging of Reaction Control Jets and Backshell Aeroheating of Orion Capsule. *J. Spacecr. Rocket.* **2015**, *52*, 243–252. [CrossRef]
31. Sansica, A.; Sandham, N.; Hu, Z. Forced response of a laminar shock-induced separation bubble. *Phys. Fluids* **2014**, *26*, 093601. [CrossRef]
32. Dolling, D.S. Fifty Years of Shock-Wave/Boundary-Layer Interaction Research: What Next? *AIAA J.* **2001**, *39*, 1517–1531. [CrossRef]
33. Hoffman, E.N.A.; Rodriguez, J.M.; Cottier, S.M.; Combs, C.S.; Bathel, B.F.; Weisberger, J.M.; Jones, S.B.; Schmisseur, J.D.; Kreth, P.A. Modal Analysis of Cylinder-Induced Transitional Shock-Wave/Boundary-Layer Interaction Unsteadiness. *AIAA J.* **2022**, *60*, 2730–2748. [CrossRef]
34. Estruch, D.; MacManus, D.G.; Richardson, D.P.; Lawson, N.J.; Garry, K.P.; Stollery, J.L. Experimental study of unsteadiness in supersonic shock-wave/turbulent boundary-layer interactions with separation. *Aeronaut. J.* **2010**, *114*, 299–308. [CrossRef]
35. Combs, C.S.; Lash, E.L.; Kreth, P.A.; Schmisseur, J.D. Investigating Unsteady Dynamics of Cylinder-Induced Shock-Wave/Transitional Boundary-Layer Interactions. *AIAA J.* **2018**, *56*, 1588–1599. [CrossRef]

36. Clemens, N.T.; Narayanaswamy, V. Low-Frequency Unsteadiness of Shock Wave/Turbulent Boundary Layer Interactions. *Annu. Rev. Fluid Mech.* **2014**, *46*, 469–492. [CrossRef]
37. Murphree, Z.R.; Combs, C.S.; Yu, W.M.; Dolling, D.S.; Clemens, N.T. Physics of unsteady cylinder-induced shock-wave/transitional boundary-layer interactions. *J. Fluid Mech.* **2021**, *918*, A39. [CrossRef]
38. Combs, C.S.; Schmisseur, J.D.; Bathel, B.F.; Jones, S.B. Unsteady Analysis of Shock-Wave/Boundary-Layer Interaction Experiments at Mach 4.2. *AIAA J.* **2019**, *57*, 4715–4724. [CrossRef]
39. Combs, C.S.; Kreth, P.A.; Schmisseur, J.D.; Lash, E.L. Image-Based Analysis of Shock-Wave/Boundary-Layer Interaction Unsteadiness. *AIAA J.* **2018**, *56*, 1288–1293. [CrossRef]
40. Sun, Z.; Gan, T.; Wu, Y. Shock-Wave/Boundary-Layer Interactions at Compression Ramps Studied by High-Speed Schlieren. *AIAA J.* **2020**, *58*, 1681–1688. [CrossRef]
41. Dolling, D.S.; Or, C.T. Unsteadiness of the shock wave structure in attached and separated compression ramp flows. *Exp. Fluids* **1985**, *3*, 24–32. [CrossRef]
42. Kreth, P.A.; Gragston, M.; Davenport, K.; Schmisseur, J.D. Design and Initial Characterization of the UTSI Mach 4 Ludwieg Tube. In Proceedings of the AIAA Scitech 2021 Forum, Virtual, 11–21 January 2021. [CrossRef]
43. Cobourn, J.W. Optical Measurements of Viscous Interactions on a Hollow-Cylinder/Flare in a Mach 4 Freestream. Master's Thesis, The University of Tennessee, Knoxville, TN, USA, 2020.
44. Settles, G.; Covert, E. *Schlieren and Shadowgraph Techniques: Visualizing Phenomena in Transport Media*; Springer Science & Business Media: Berlin/Heidelberg, Germany, 2001. [CrossRef]
45. Willert, C.E.; Mitchell, D.M.; Soria, J. An assessment of high-power light-emitting diodes for high frame rate schlieren imaging. *Exp. Fluids* **2012**, *53*, 413–421. [CrossRef]